

SMHI

Meteorologi

SMHI Ex 2

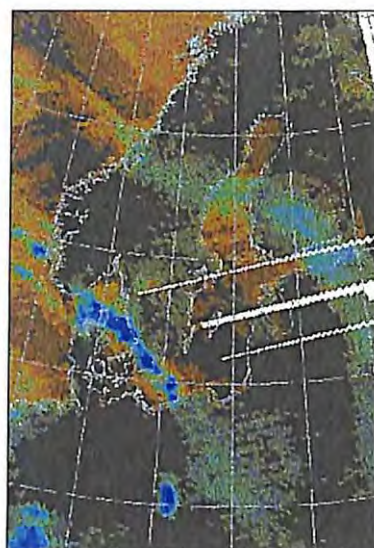
Nr 93, 1999

BIBLIOTEKET
2001-04-26

Swedish Meteorological and Hydrological
Institute

Nowcasting SAF

Precipitation Analysis from AMSU



*Ralf Bennartz
Anke Thoss
Adam Dybbroe
Daniel B. Michelson*

Visiting scientist report

November 1999

Acknowledgements

This work was performed during a 2-month visiting scientists stay of Ralf Bennartz at the Swedish Meteorological and Hydrological Institute within the framework of EUMETSAT's Nowcasting Satellite Application Facility.

Front image

The front cover shows the visualization of the precipitation classification for September, 23rd 1999, 17:24 UT. The left image shows the radar reflectivity observed from the BALTRAD network. The right image gives the result of the precipitation classification, where the class 1 (risk/light precipitation) is assigned red, class 2 (light/moderate) green, and class 3 (intensive precipitation) blue. Two different precipitation areas can be observed. The southern part of the Baltic region is covered with a narrow band of intensive precipitation, whereas more widespread frontal precipitation is found in the northern part. Both the light and the intensive precipitation are picked up by the AMSU and their respective intensity can also be distinguished very clearly.

Abstract

We describe a method to remotely sense precipitation and classify its intensity over water, coast, and land surfaces. This method is intended to be used in a nowcasting environment. It is based on data obtained from the Advanced Microwave Sounding Unit (AMSU) onboard NOAA-15. Each observation is assigned a probability to belong to four different classes, namely precipitation-free, risk of precipitation, precipitation between 0.5 and 5 mm/h and precipitation higher than 5 mm/h. Since the method is designed to work over different surface types, it mainly relies on the scattering-signal of precipitation-sized ice particles received at high frequencies.

For the calibration and validation of the method we use an eight month dataset of combined radar and AMSU-data obtained over the Baltic area. We compare results for the AMSU-B channels at 89 GHz and 150 GHz and find that the high frequency channel at 150 GHz allows for a much better discrimination of different types of precipitation than the 89 GHz channel. While precipitation-free areas as well as heavily precipitating areas ($> 5\text{ mm/h}$) can be identified to a high accuracy, the intermediate classes are more ambiguous. This ambiguity stems from the ambiguity of the passive microwave observations as well as from the non-perfect matching of the different data sources and non-perfect radar adjustment. In addition to a statistical assessment of the method's accuracy, we present case studies to demonstrate its capabilities to classify different types of precipitation and to seamlessly work over highly structured, inhomogeneous surfaces.

Contents

1	Introduction	4
2	Dataset	5
2.1	The Advanced Microwave Sounding Unit (AMSU)	5
2.2	Combined satellite and radar dataset	7
2.3	BALTRAD radar data	7
3	Algorithm description	8
3.1	General	8
3.2	Land/water discrimination	11
3.3	Land surfaces	12
3.3.1	Snow and ice screening	13
3.3.2	Precipitation identification	13
3.4	Water surfaces	17
3.4.1	Emission signal	17
3.4.2	Scattering signal	19
3.5	Coast	21
4	Case studies	21
4.1	Case 1	22
4.2	Case 2	23
4.3	Case 3	26
5	Summary and conclusions	28
A	Algorithm description for scattering-based precipitation identification	31
A.1	Land	31
A.1.1	AMSU-A water or coast, AMSU-B land:	31
A.1.2	AMSU-A land (and AMSU-B land):	31
A.2	Sea	31
A.2.1	AMSU-A land or coast, AMSU-B water:	31
A.3	Coast	32
B	Software and data formats	32
B.1	Convolution of land/sea-mask	32
B.2	Backus-Gilbert convolution of AMSU-B to AMSU-A	33
B.3	Retrieval software	34
B.4	Flags	35

1 Introduction

At the Swedish Meteorological and Hydrological Institute (SMHI) methods and software to retrieve cloud and precipitation information from the data of the new generation of operational meteorological satellites is being developed. The work is carried out mainly in the framework of EUMETSAT's 'Satellite Application Facility (SAF) to Support Nowcasting and Very Short Range Forecasting'. The Nowcasting SAF (SAFNWC) is scheduled to end in February 2002, with the delivery of an integrated software package for the processing of twelve analysis products, all thought to be essential for nowcasting applications, and based on data of the future Meteosat Second Generation (MSG) and European Polar System (EPS) satellites.

The main delivery of SMHI will be new methods and software for the extraction of four high latitude (applicable north of 50N) cloud and precipitation products based on AVHRR and AMSU data. *Karlsson et al.* (1999) give a short overview of the four products and the AVHRR Cloud Mask is described in more detail by *Dybbroe et al.* (1999).

In this paper we will describe a method to identify precipitation and classify its intensity over water, coast and land surfaces using AMSU data. The method is going to be an important part of the algorithm for the AVHRR/AMSU Precipitating Clouds product of the SAFNWC.

Satellite based precipitation analysis for nowcasting purposes impose specific requirements:

- The spatial resolution of the product should be as high as possible. Therefore, the discrimination between precipitating and non-precipitating clouds has to work on an individual pixel basis over both, land and water surfaces. In contrast, e. g. climate applications need an integral measure of precipitation's distribution over larger grid boxes and periods. Climate products might thus still be useful, if a large amount of individual retrievals fail, as long as temporal and spatial averages are correct.
- A high accuracy in determining the absolute amount of precipitation for a given pixel is not necessarily required for nowcasting. An optimal interpretation of a nowcasting product would distinguish between a few classes of precipitation intensities ranging from precipitation-free to intensive precipitation. The usefulness of climate products in contrast depends on their ability to derive precipitation intensity to a very high accuracy.

Current operational satellites such as NOAA-15 carry two different kinds of instruments which are of potential interest for the remote sensing of precipitation. Visible and infrared sensors such as the Advanced Very High

Resolution Radiometer (AVHRR) and microwave instruments such as the Advanced Microwave Sounding Unit (AMSU). While the AVHRR provides a high spatial resolution (in the order of 1 km at nadir), the observed radiances in this spectral region are not sensitive to the precipitation itself and precipitation information has to be derived from indirect measures such as the cloud optical properties, cloud top temperature or cloud type. A typical problem associated with visible and infrared methods is that they can not distinguish between cold thick clouds with and without precipitation and thus typically overestimate the areal extent of precipitation.

Passive microwave instruments provide a more direct measure of precipitation, since precipitation directly influences the radiation field. To fully meet the above requirements and to obtain a high skill in correctly identifying precipitation, the use of passive microwave information is thus necessary. The drawback of passive microwave instruments is their low spatial resolution of typically several 10th of kilometers. Previous studies have further shown that for instantaneous observations the assignment of passive microwave observations to rain rates is associated with large error bars. Therefore we introduce a new approach that distinguishes between different classes of precipitation instead of deriving rain rates. To also allow the user to estimate the uncertainties associated with a given classification, we derive the results in terms of probabilities of a given observation belonging to each class. These probabilities are derived from the co-located and gauge-adjusted radar data.

In the following section we will give a short description of the here-relevant features of the AMSU and of the dataset we used. In section 3 we will describe the classification approach in detail and perform a statistical evaluation of its accuracy with respect to the radar data. In section 4 we provide case studies for different types of precipitation to highlight the capabilities of the method and identify possible error sources.

2 Dataset

2.1 The Advanced Microwave Sounding Unit (AMSU)

The AMSU consists of two instruments, AMSU-A and AMSU-B. While the former is dedicated to derive temperature profile information, the main purpose for AMSU-B is the retrieval of water vapour profile information. Both instruments are cross-track scanning, where the AMSU-A swath consists of 30 measurements (step angle 3.3 degrees) and the AMSU-B swath of 90 measurements (step angle 1.1 degree). During one AMSU-A scan three AMSU-B scans are performed. Both instruments are synchronized via a pulse at the beginning of each AMSU-A scan. The spatial resolution

AMSU-A		
spatial resolution	deg	3.3
nadir effective field of view	km^2	50x50
scan edge effective field of view	km^2	150x80
channels used	[GHz]	23.8, 31.4
AMSU-B		
spatial resolution	deg	1.1
nadir effective field of view	km^2	20x16
scan edge effective field of view	km^2	64x52
channels used	[GHz]	89.0, 150.0

Table 1: NOAA-15 satellite characteristics and AMSU-A and AMSU-B instrument characteristics taken from the NOAA KLM User's Guide (Goodrum et al., 1999) and (Bennartz, 1999b).

of the AMSU-A varies between $50 \times 50 km^2$ (3-db effective field of view) at the scan center to $150 \times 80 km^2$ at scan edge. AMSU-B has a somewhat higher spatial resolution of $20 \times 16 km^2$ at scan center and $64 \times 52 km^2$ at scan edge. Details on the spatial resolution and observation geometry of the AMSU can be found in (Goodrum et al., 1999) and (Bennartz, 1999b) (see also Table 1).

Both AMSU-A and AMSU-B have window channels, the AMSU-A at 23.8, 31.4, and 89.0 GHz, whereas the AMSU-B at 89.0 and 150.0 GHz. These channels are most suitable to obtain information about precipitation since they are least affected by water vapour or oxygen absorption.

The response of the AMSU window channels to precipitation is qualitatively well known Smith et al. (1998), while an exact quantitative relation between surface rain rate and observed brightness temperatures is difficult to establish.

Considering the microwave response to precipitation two different signals have to be distinguished. First, liquid precipitation acts as an almost unpolarized emitter, so that the over cold, polarized targets (i. e. ocean surface) liquid precipitation tends to brighten and depolarize the satellite-observed temperatures. This effect can especially be observed at low frequencies (AMSU-A 23.8 and 31.4 GHz) and its use is limited to open water surfaces, since most land surfaces exhibit a too high and variable surface emissivity.

The second effect is a depression of the observed brightness temperatures which is largely caused by precipitation-sized ice particles (Spencer et al., 1989; Grody, 1991; Adler et al., 1993). At high frequencies these large ice particles act as scatterers and scatter cold radiation from above the cloud back to the satellite. While only indirectly linked with surface precipitation, the scattering signal can be observed both over land and water sur-

faces. For the special case of the AMSU the usage of the higher AMSU-B frequencies is advantageous because of its approximately three times higher spatial resolution. AMSU-B will therefore have a more dynamic response to precipitation features, especially, if the areal extent of the precipitation is small.

2.2 Combined satellite and radar dataset

In the framework of the SAFNWC SMHI has been building a database for validating satellite retrievals of precipitation at high latitudes. As of November 1999 this dataset consists of 140 NOAA-15 overpasses received at Norrköping along with coinciding weather radar data (see section 2.3). The dataset is currently operationally extended on a daily basis and will at least be extended until one year of data coverage is obtained. The locally received NOAA-15 data is processed using the Advanced ATOVS Processing Package (AAPP, *Klaes (1997)*).

Since the weather radar data are available at a much higher spatial resolution as the AMSU-data, we convolved the high-resolution datasets to the spatial resolution of the AMSU-A respective AMSU-B. This degradation allows to intercompare the radar and AMSU data on an instantaneous basis and at a common spatial scale. The principal strategy for degrading high-resolution datasets to the resolution of passive microwave sensors is outlined in *Bennartz (1999a)* and *Bennartz and Michelson (1999)*. Subsequently we give a short description of the weather radar dataset.

2.3 BALTRAD radar data

The Baltic Sea Experiment (BALTEX) is the European regional project within the Global Energy and Water Cycle Experiment (GEWEX), with contributions from 10 countries in the Baltic Sea's drainage basin. GEWEX is part of the World Climate Research Programme. The BALTEX Main Experiment commenced its so-called Pilot Phase on April 1, 1999. The BRIDGE Base-Line Period commenced on October 1, 1999 and is presently scheduled to last until February 28, 2002 (*BALTEX, 1997*).

Within the framework of BALTEX, a Radar Data Centre (BRDC) has been established at SMHI for collecting data from as many radars in or proximate to the BALTEX Region as possible, deriving homogenous data sets, distributing the datasets to BALTEX data users, and archiving the datasets. During the BRIDGE Pilot Phase, data was available from 25 radars in six countries. Most of these radars operate at C-band (5 cm), while two operate at X-band (3 cm). The majority of the radars have Doppler capability. Their maximum operational ranges are 200-250 km and the horizontal resolution

of the data is commonly 2 km. With the exception of four radars which produce reduced depth data, reflectivity factor data (dBZ) is available in 8-bit depth. More information on the radars targeted for use in BALTEX can be found in *Brandt et al.* (1996).

Those products being produced at the BRDC are outlined in *Michelson et al.* (1999) and presented in detail in *Michelson* (2000). Among them is a 12-hour accumulated precipitation product based on gauge-adjusted radar. The gauge-adjustment technique is based on that presented by *Koistinen and Puhakka* (1981), with a few modifications. Gauge observations from SYNOP were used for 6 and 18 UTC each day. Based on 15 minute Pseudo-CAPPI images, twelve hour radar sums for each radar were derived for the corresponding integration periods and these were composited; a composite of images containing surface distances from each radar's location for each radar was also created. A second order polynomial was then fitted for $\log(\text{Gauge sum/Radar sum})$ as a function of distance. In order to avoid overfitting, this relation was derived using a moving one-week window comprising all gauge-radar pairs along with their corresponding distances. This was conducted with every new 12-hour SYNOP term. This relation was used as a first guess in a Barnes' analysis which generated an adjustment field which was applied to the original radar accumulation composite. The coefficients for the polynomials were written to a log file for later use. The gauge-adjustment technique has the effect of minimizing the range dependency on the radar sum's accuracy while marginalizing the bias between radar and gauge accumulations on the whole (*Michelson*, 2000). The polynomial coefficients can be used to perform a simpler adjustment of radar data for arbitrary temporal integrations periods between SYNOP terms.

For the purposes of this study, single composite images containing radar reflectivity factor (dBZ) were converted to rain rate (mm/h) using a static Z-R relation $Z = 200R^{1.5}$ and then adjusted using the corresponding set of polynomial coefficients and information on the distance from each pixel to the nearest radar. While the composites themselves are not created using a closest radar algorithm, the effects on the radar data accuracy can be considered marginal, especially in light of the difference in their resolution compared with the AMSU data.

3 Algorithm description

3.1 General

Figure 1 outlines the general data flow of the precipitation retrieval. Since land and water surfaces exhibit an entirely different emissivity and also the

response of passive microwave brightness temperatures to precipitation differs considerably, the first step is to discriminate between land and water surfaces. As the spatial distribution of land and water is highly inhomogeneous in the Baltic region an accurate determination of the viewed scene is of crucial importance to avoid a large amount of falsely classified pixels in coastal areas. Since the spatial resolution of the AMSU is very low, it is further necessary to define a particular surface type for coastal observations, which are partly covered by land and water. The subsequent processing of the AMSU-data depends on the type of surface. Correspondingly, the precipitation identification is different for the different surface types.

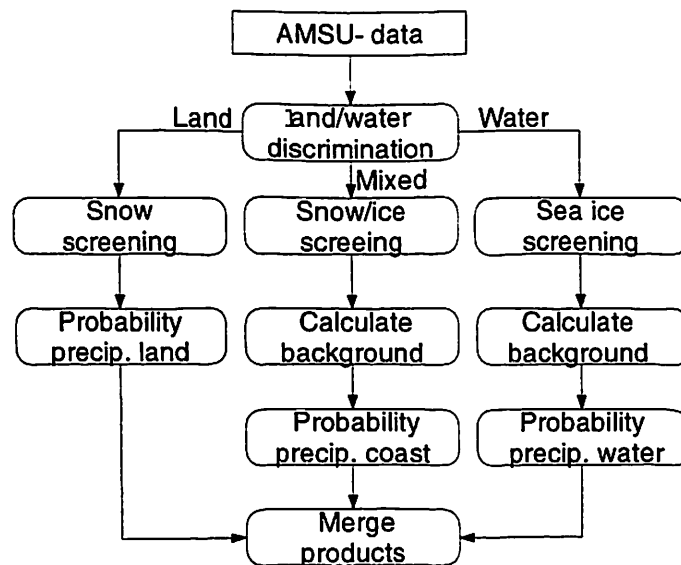


Figure 1: Algorithm overview.

Instead of deriving precipitation rates, the final product of the here-described method are probabilities that a given observation falls within certain, predefined ranges of rain rates. Table 2 shows the different classes which we use. A given pixel will not be assigned a certain value, it will rather be assigned a set of probabilities with which it belongs to each of the four classes, where the sum of these probabilities adds up to 100%. Although a larger number of precipitation classes would be useful the validation results presented below indicate that on an instantaneous basis and over all different surface types the algorithm's accuracy does not allow to discriminate more classes.

Our approach to derive the probabilities associated with different classes of precipitation is strictly empirical. We use the convolved radar data to

class	type of precipitation	minium rain rate	maximum rain rate
		[mm/h]	[mm/h]
1	No precipitation	0.0	0.1
2	Risk for/light precipitation	0.1	0.5
3	Light/moderate precipitation	0.5	5.0
4	Intensive precipitation	5.0	∞

Table 2: Classes of different precipitation intensities used in this investigation.

discriminate between the different classes of precipitation and investigate the skills of different combinations of AMSU-channels to discriminate between those classes (note, that all algorithms are outlined in Appendix A). We chose this approach instead of e. g. an inverse modelling approach since the microwave response to e. g. frozen precipitation as well as the cloud microphysics is not yet well understood and may introduce large systematic deviations in algorithm development especially in the here-presented case, where surface characteristics are highly heterogeneous. For a detailed discussion on the response of passive microwave sensors to frozen precipitation see *Bennartz and Petty (1999)*. While in principle straight forward, the empirical approach has several limitations:

1. The so-derived thresholds and probabilities may not be valid for other climate regions than those for which they have been derived. It might thus be difficult to transfer the here-derived technique without adjustment to other climate regions. This might especially be the case for the algorithms which are derived over water, since the response of passive microwave sensors to other atmospheric parameters is stronger over ocean than over land. For land surfaces problems could arise in regions with significantly different surface emissivity characteristics, such as desert areas.
2. If the number of observations is limited the results may not be statistically significant or may be biased towards a non-representative sample of data. In the present investigation we used data collected over a period of eight month (April-November 1999), so that for most seasons a good coverage is obtained. However, as outlined below, the dataset will be extended to cover at least one year of data to include a larger amount of winter time situations as well.
3. The usage of radar as ground truth introduces additional errors in the comparison. First, because a perfect alignment in time of the weather radar data with the passive microwave data can not be obtained. Although the time difference between radar data and AMSU-data was

7.5 minutes at maximum, rapidly developing thunderstorms may have significantly changed their state within this time frame. Secondly, the navigation of the satellite may introduce errors in the spatial collocation of the radar and AMSU-data. Thirdly, the radar data itself may not always represent the actual surface rain rate, neither will it be completely free of artefacts, such as anomalous propagation or ground clutter. Illustrations of all of these problems can be found in the case studies (section 4). Despite these problems radar remains the only source to intercompare with passive microwave data on a pixel-by-pixel basis, since other observing systems as e. g. rain gauges are not capable to resolve the spatial and temporal distribution of the precipitation.

3.2 Land/water discrimination

The land water discrimination is done using the method outlined in *Bennartz* (1999a). The fraction of water surfaces within each passive microwave footprint is derived by degrading a high-resolution land/sea mask to the actual resolution of the passive microwave sensor. *Bennartz* (1999a) shows that the accuracy with which the fraction of land surfaces can be determined mainly depends on the navigation errors of the satellite data. If the navigation of the satellite data is not correct, systematic errors in the determination of the fraction of land in the pixel might be introduced. Figure 2 shows the dependence of the AMSU-A brightness temperatures on the fraction of land surface within the microwave footprint. To highlight the issue of land/sea discrimination Figure 2 shows results of an overpass, where only little precipitation occurred (as outlined below precipitation identification over coastal areas can be thought of as interpreting the deviations from the relation between the land fraction and the observed brightness temperatures shown in Figure 2). The observed variability for homogeneous land surfaces (i. e. land fraction equal one) is caused by variations in land surface temperature and surface emissivity, while the variability for homogeneous water surfaces is mainly caused by variations in atmospheric parameters, namely columnar water vapour, cloud liquid water, and surface wind speed. For mixed land/water pixels the variability is caused by an overlap of both, the atmospheric and land surface parameters. Note, that on the scale of the AMSU-A no homogeneous land surfaces are found in the Baltic region, and only very few homogeneous water pixels in the center of the Baltic proper. For the AMSU-B this statement holds as well although to a lesser extent, so that for both the handling of coastal observations is of crucial importance.

To delineate between homogeneous water surfaces, land surfaces and coastal zones, we set thresholds on the fraction of land which is allowed to occur within a given footprint. Measurements were labeled homogeneous

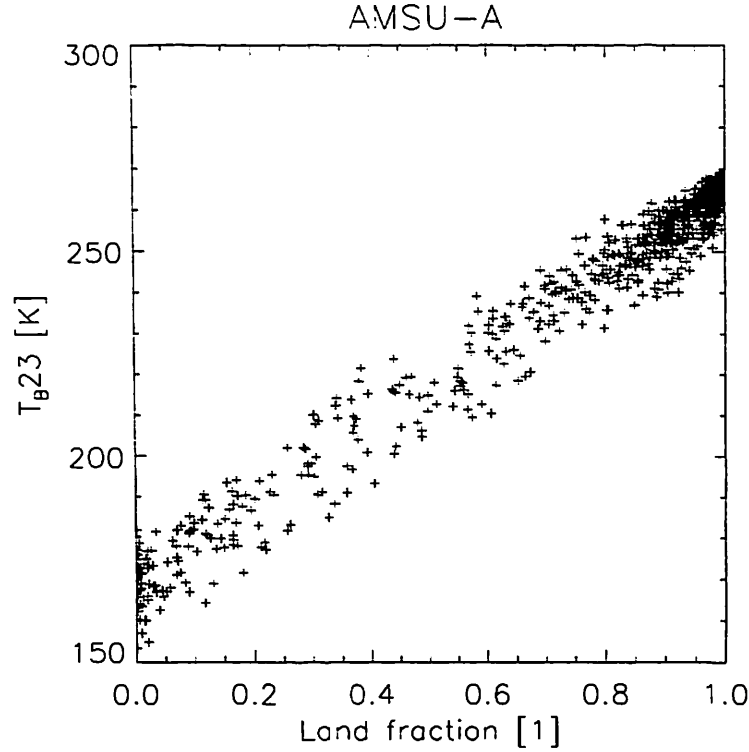


Figure 2: Dependence of the AMSU-A brightness temperatures at 23.8 GHz on the fraction of land surface in the footprint.

water, if the fraction of land was less than 1%. This threshold corresponds to a maximum systematic contamination of the observed brightness temperature at 23.8 GHz of 0.9 K, given the sensitivity of 0.9 K/percent which can be observed in Figure 2.

For the high frequency channels, where the contrast between land and water is smaller, the deviation is smaller. For land surfaces we chose a less conservative threshold of 95%, so that all pixels with a land fraction higher than 95% were considered homogeneous land. The remaining pixels between 1% and 95% land fraction are considered coastal. Table 3 gives the total number of AMSU-A and AMSU-B observations within the BALTRAD coverage area and the relative number of water, coast, and land pixels according to the above classification.

3.3 Land surfaces

Over high emissivity land surfaces the impact of the signal of atmospheric emitters such as water vapour, cloud liquid water and liquid precipitation on the observed brightness temperatures is very small. Precipitation identi-



	Total pixels	Land	Coast	Water
		[%]	[%]	[%]
AMSU-A	115165	43.8	50.0	6.2
AMSU-B	1046797	50.5	37.9	11.6

Table 3: Total amount of data used in this investigation.

fication thus solely relies on the scattering signal of precipitation-sized ice particles.

3.3.1 Snow and ice screening

Snow cover or glacial ice on land surfaces causes a signal at high frequencies similar to that of frozen precipitation and may thus result in consistent mis-classifications. In winter time conditions it is therefore of major importance to first screen for snow/ice cover before precipitation information is retrieved. We currently employ the scheme described in *Grody et al.* (1999) to screen for snow and ice covered surfaces. However, since our current validation dataset only covers very few cases (four overpasses in April 1999) with significant amount of snow-covered surfaces, we were not able to validate the scheme with statistical significance. Figure 3 shows one of the overpasses where the northern most parts of Scandinavia and the Norwegian mountains were covered with snow. The left image shows the complete rgb-image, where the snow-covered parts can be identified as blue areas over land surfaces. The right image displays the result of the snow identification, where except for very few pixels all the snow-covered areas were removed.

Besides the use of the aforementioned tests defined by *Grody et al.* (1999), work of *Bauer and Grody* (1995) suggests that the additional use of water vapour sounding channels might enhance the discrimination snow cover and rainfall. These results are indeed supported by our observations (e. g. Figure 3), where snow-covered areas exhibit a higher brightness temperature at $183 \pm 7 \text{ GHz}$ than at 150 GHz, since the emission of water vapour tends to brighten the absorption channel more than the window channel. Since the discrimination of snow-covered surfaces from precipitation is of major importance for mid- and high-latitude winter conditions, we will revisit this issue as soon as we have collected a large enough dataset of co-located radar and AMSU data for winter time conditions.

3.3.2 Precipitation identification

Over land surfaces the isolation of the scattering signal is simply performed using the difference between a low-frequency channel (AMSU-A 23.8 GHz)

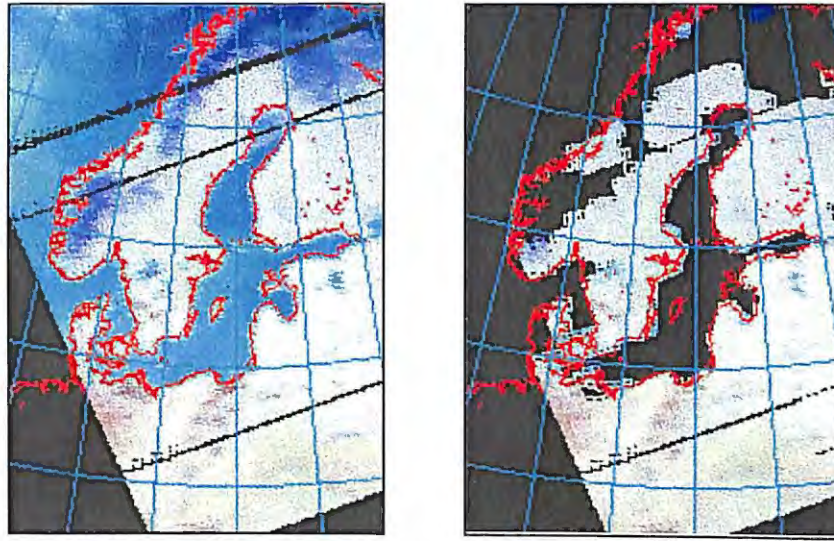


Figure 3: Example for the ice detection over land. The left panel shows an rgb-composite of the AMSU-B channels at 89 GHz (red), 150 GHz (green), and 183 ± 7 GHz blue and the right panel shows the same image with sea and snow-cover removed.

and a high frequency channel (89 GHz or 150 GHz), we refer to these difference as the scattering index at 89 GHz respective 150 GHz (see Equation (2)). For non-precipitating situations this difference will be around zero, whereas for precipitating situations it will increase to values of higher than 50 K, dependent on the total amount of precipitation-sized ice in the field of view.

The likelihood with which a given observation belongs to one of the above defined four different classes (see Table 2) may be derived by using the radar data to sub-divide the complete dataset into four classes according to their respective thresholds in rain rates. From these data we derived histograms of the distribution of the scattering index for each of the four classes. Figure 4 (upper panel) shows the histograms normalized to a peak value of 100 for the 89-GHz scattering index. From the histograms we derived the likelihood for which a given scattering index belongs to a certain class under the constraint that for each scattering index the total probability has to be 100%. The resulting likelihood estimates are shown in Figure 4 (lower panel). While the classes 1 (no precipitation) and 4 (precipitation greater than 5mm/h) can be separated, the classes 2 and 3 overlap strongly

with each other and with classes 1 and 4. Only for scattering indices between zero and 2 K class 2 has slightly higher probabilities than class 3.

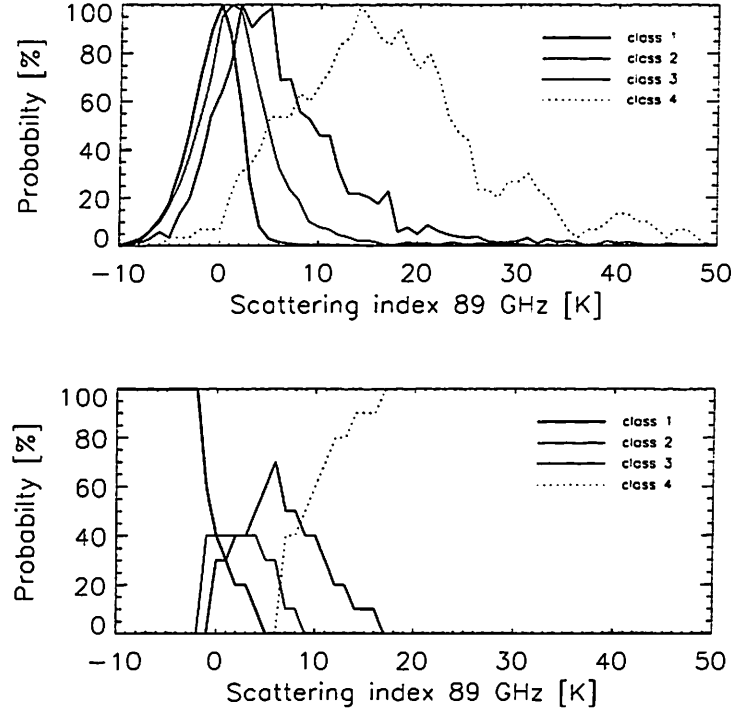


Figure 4: The upper panel shows histograms (normalized to a peak value of 1) of the distribution of the scattering index at 89 GHz for the four classes. The observations were classified according to the radar-derived, convolved rain rate. The lower image give the probabilities with which a given scattering index belongs to a certain class. These are derived from normalizing the histograms (upper panel) to add up to 100% for a each scattering index.

The separation of the four classes can be enhanced if the 150 GHz channel is used instead of the 89 GHz channel. Figure 5 shows the histograms and corresponding likelihoods for the 150 GHz scattering index. One can see that the separation between the classes 1 and 4 has now increased from 1 K (Figure 4 (lower panel)) to 6 K. Also the likelihood of classifying a given observation as class 2 or 3 has increased in the range between zero and 7 K scattering index.

To further evaluate the benefit of using the 150 GHz scattering index and also to highlight the problems in the identification of light precipitation, we performed a hard clustering on the maximum likelihood estimates derived for the entire dataset over land. Hard clustering in this context means that we assign each pixel the class which has the maximum likelihood of occurrence

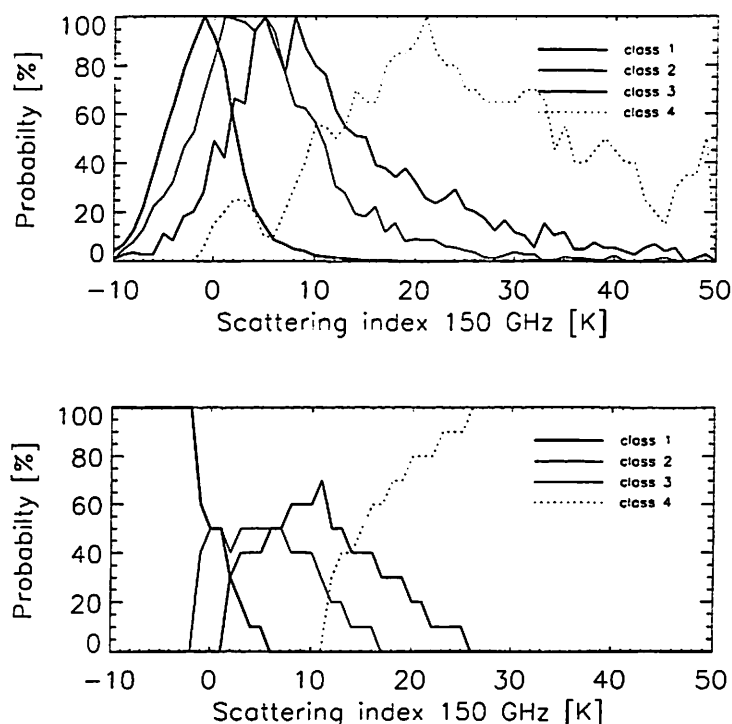


Figure 5: As Figure 4 but for the 150 GHz scattering signal over land.

(i. e. discriminating between the classes using fixed thresholds). From this hard clustering results we derived contingency tables for both the 89 and 150 GHz scattering indices. Table 4 summarizes the results.

Note, that the results given in this and the following contingency tables can not be seen as a validation or quality assessment of the passive microwave remote sensing techniques, since they are deteriorated by the above described problems with navigation, radar adjustment, clutter removal etc. Despite this, we find it useful to provide this information since it reflects the degree of agreement between two independent, though non-perfect, observation techniques without having the possibility to give an absolute measure on the accuracy of either one. Further the relative benefits of different passive microwave channel approaches may be evaluated. The use of 150 GHz especially allows a much more unambiguous identification of precipitation-free areas than the 89 GHz based method. While for 89 GHz about 15% of the precipitation-free areas are falsely classified as precipitation (14.8% in class 3 and 0.4% in class 3), this occurs only for about 2.6% (2.4% class 3 and 0.4% class 4) when using 150 GHz. The ambiguous results for classes 2 and 3 for both indices highlight the necessity to associate an uncertainty estimate with any given observation. This is indeed the main reason why

classified as/ belongs to	measurements in class	class 1 [%]	class 2 [%]	class 3 [%]	class 4 [%]
class 1	42943	51.0	33.8	14.8	0.4
class 2	3526	28.0	25.5	40.6	5.9
class 3	2516	12.0	12.9	45.4	29.7
class 4	129	0.7	1.6	14.0	83.7
classified as/ belongs to	measurements in class	class 1 [%]	class 2 [%]	class 3 [%]	class 4 [%]
class 1	42943	76.6	20.8	2.4	0.2
class 2	3526	31.1	33.9	26.7	8.3
class 3	2516	9.9	22.1	36.1	31.9
class 4	129	0.9	3.6	12.7	82.8

Table 4: Contingency table for the four different classes over land. The upper table gives the results for the 89 GHz scattering index, the lower table those for the 150 GHz scattering index.

our final product is the likelihood for each pixel to belong to a certain class instead of a hard clustering. It is obvious that unambiguous decision on whether light precipitation occurs in a certain area can not be taken from the scattering index alone. Therefore we feel this ambiguity has to be resembled in the product which is delivered to the user who then can use the likelihoods together with other data sources available in e. g. mesoscale analysis systems.

3.4 Water surfaces

At high latitudes over water surfaces a screening for possible sea ice has to be performed. We currently employ the sea ice screening of *Grody et al.* (1999). Since our current validation dataset does not cover sea ice, a complete validation of this scheme has to be postponed until a sufficiently large dataset including sea ice is collected. We can however say that the screening does not produce any false sea ice signatures in our current (sea-ice-free) dataset.

Two commonly used ways to identify precipitation over ocean are tested based on the aforementioned emission and scattering signals.

3.4.1 Emission signal

Cloud liquid water derived from the low frequency channels of the AMSU-A may be used to identify situations where liquid water path exceeds a certain threshold. Since large rain droplets lead to a strong increase in optical depth, liquid water path increases rapidly in presence of a significant amount

of liquid precipitation. We adapt this technique for the AMSU-A using the liquid water retrieval algorithms specified in *Bennartz et al. (1997)*. The drawback of this algorithm is that it can only be applied to AMSU-A and the coarse spatial resolution of the AMSU-A hampers both, the application and the verification. On the scale of the AMSU-A the retrieval becomes more problematic, since the precipitation intensity is much smaller on a $50 \times 50 \text{ km}^2$ scale than on AMSU-B's $15 \times 20 \text{ km}^2$ scale. Figure 6 illustrates this problem. It shows the radar-derived rain rates convolved to the resolution of AMSU-b against the same data convolved to the resolution of the AMSU-A for all pixels over sea.

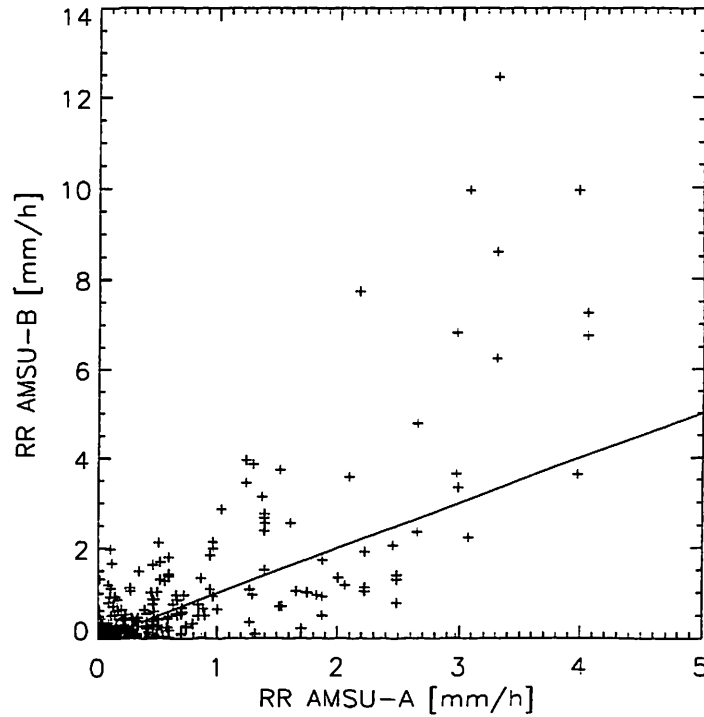


Figure 6: Radar-derived precipitation intensity convolved to the spatial resolution of AMSU-B versus the same convolved to the spatial resolution of the AMSU-B

The maximum rain rate that occurs at AMSU-A resolution is about 4mm/h, whereas at AMSU-B maximum rain rates exceed 10mm/h. A validation of the emission based algorithm is further complicated by the fact that only 6% of the validation dataset can be considered as homogeneous water surface at the spatial scale of AMSU-A (see Table 3). The obvious conclusion from this is that we do not have any measurements that fall into the above defined class 4 (see Table 2). We can therefore only derive infor-

mation about the classes 1 to 3.

The histograms derived for the emission signal are presented in Figure 7. Since the number of points in the dataset is much smaller than for the above discussed screening over land, the histograms (Figure 7, upper panel) are much more noisy than those derived for land. The transition between class 1 and class 2 occurs for a liquid water path of 0.05 kg/m^2 , whereas for a threshold around 0.3 kg/m^2 class 3 becomes most likely. Interestingly, the latter is identical with the threshold value given in *Grody et al. (1999)* to discriminate between rain and no rain, although both, the retrieval algorithms for cloud liquid water and the approach to derive the threshold are different.

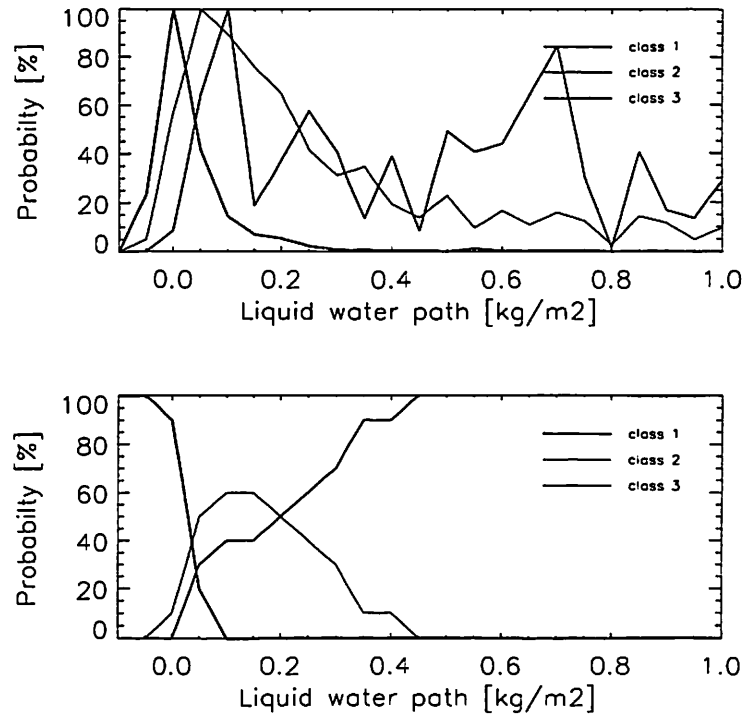


Figure 7: As Figure 4 but for emission signal over sea.

3.4.2 Scattering signal

As for land surfaces the different window channels of the AMSU-A and AMSU-B may be used in different combinations to obtain scattering indices. For the work presented here, we tried the combination $T_{23} - T_{89}$, $T_{23} - T_{150}$, and $T_{89} - T_{150}$. Although, both the 89 GHz channel and the 150 GHz channel are affected by scattering, the latter one turned out to give

classified as/ belongs to	measurements in class	class 1 [%]	class 2 [%]	class 3 [%]	class 4 [%]
class 1	34176	82.8	15.8	1.4	0.0
class 2	3503	15.6	54.0	28.4	2.0
class 3	2295	3.7	31.2	48.2	16.9
class 4	94	1.3	6.7	25.3	66.7

Table 5: As Table 4, but for sea.

the best results. Another advantage of the latter channel combination is of course that both channels are on the AMSU-B resolution, whereas for all other cases including the above discussed emission type algorithm the low-frequency channels of AMSU-A are included.

Figure 8 visualizes the distribution of the observed scattering index (derived from Equation (3)) in the upper panel and the resulting probabilities assigned to a given scattering index in the lower panel. It can be seen that the dynamic range of scattering indices over water surfaces is much larger than over land surface, which also leads to better results, if a hard clustering is performed (Table 5).

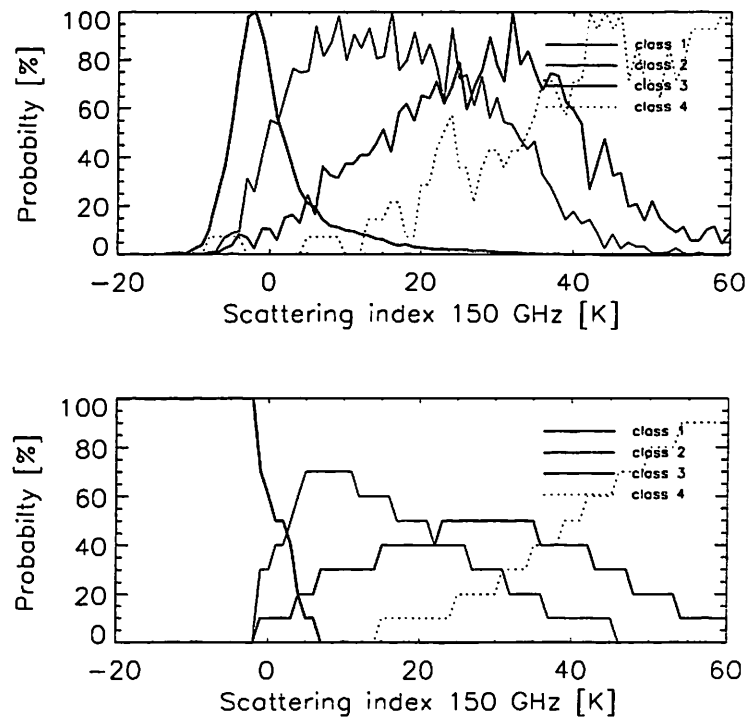


Figure 8: As Figure 4 but for 150 GHz scattering signal over sea.

classified as/ belongs to	measurements in class	class 1 [%]	class 2 [%]	class 3 [%]	class 4 [%]
class 1	130242	70.2	25.9	3.7	0.2
class 2	13860	24.0	42.4	28.4	5.2
class 3	9298	9.0	26.3	44.3	20.4
class 4	354	5.1	8.1	25.6	61.2

Table 6: As Table 4, but for coastal observations.

3.5 Coast

Coastal pixels consist of a mixed land/water signal. This influences both the observed brightness temperature, and its sensitivity to precipitation. Our approach is to explicitly account for this mixing by weighting the observed scattering index as well as the derived probabilities with the fraction of land in the footprint (see Equation (4)). Since the dependence of brightness temperatures on the fraction of land is linear (because of the validity of the Rayleigh-Jeans approximation), the linear combination of land and sea parts eliminate the dependence of the scattering index on the the fraction of land in the footprint. Figure 9 illustrates the approach. For 10% (15000 pixels) of the coastal pixels in the dataset we plotted the scattering index derived from Equation (4) against the fraction of land surface in the footprint. The lines indicate the regions where the different classes of precipitation prevail. Every observation below the lowest line would thus have a high probability to be precipitation-free and every observation above the uppermost line would have the highest probability to belong to class 4. To allow for an estimate of the accuracy of the algorithm in coastal regions we give the contingency tables for the coastal pixels of the dataset in Table 6. As could be expected, the accuracy of the classification over coast is somewhere in between that for land surfaces and for water surfaces. Note however, that as for sea and land pixels our final product does not consist of hard-clustered classes, rather it consists of probabilities.

4 Case studies

Subsequently we show three cases of different precipitation events of the combined radar and AMSU-dataset (Figures 10, 11, and 12). For all cases we display four different images. The upper left image shows the radar reflectivity obtained from the BALTRAD radar data. For daylight overpasses the upper right images shows an rgb-composite of AVHRR channel 1 (red), 2 (green) and 4 (blue) and for night time a greyscale image of AVHRR channel 4. The lower left images give an rgb-composite of the AMSU-B

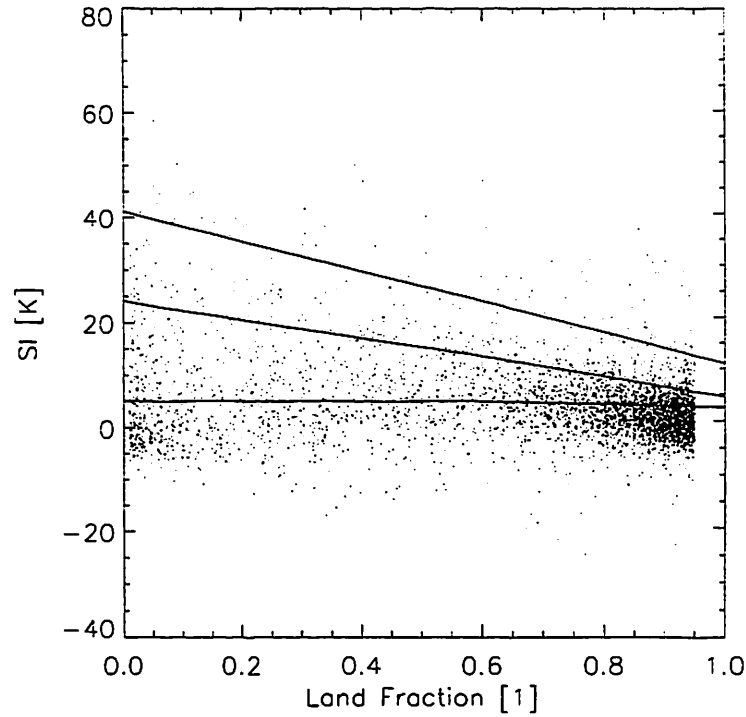


Figure 9: Visualization of the precipitation classification for coastal pixels. Shown are the scattering index derived from Equation (4) against the fraction of land observed at AMSU-B scale for 10% (15000 pixels) of the total observation over coast. The lines give the threshold values, between which the respective precipitation classes have the highest probability (e. g. below the lowermost line all observations are most likely to be precipitation-free)

channels at 89 GHz (red), 150 GHz (green) and 183 ± 7 GHz (blue). The lower right image presents the results of the precipitation classification as an rgb-image. We assigned the probabilities of the class 2 (risk for precipitation) the color red, class 3 (precipitation) green and class 4 blue. Therefore black areas indicate no precipitation whereas bright blue, green, or red areas indicate a high probability for the precipitation to fall into the associated class.

4.1 Case 1

Case 1 (Figure 10) was obtained at the 28th of June 1999, 17:45 UT. The AVHRR-imagery shows a band of intensive convective cells which extends from western Poland in the south into the Norwegian Sea in the west. The radar identifies very narrow, intensive bands of precipitation associated with

the convection. Over the western part of the Baltic Sea three separate bands of precipitation can be identified. These bands are resembled in the passive microwave precipitation classification product (Figure 10, lower right panel). Although the resolution of the AMSU is much lower than the radar's resolution the narrow band of intensive precipitation with its northern tip at Öland is identified quite accurately. The westernmost band is also quite nicely resembled, however the middle band is only assigned a risk for precipitation (reddish colors).

Comparing the areal extend of the precipitation derived from passive microwave (or radar) with that of the convective clouds shown in the upper right panel, it can clearly be seen that only parts of the convective cells exhibit intensive precipitation, whereas large parts of the clouds are precipitation-free. Although the spatial resolution of the AVHRR is much higher than that of AMSU, non-precipitating and precipitating areas within thick possibly precipitating clouds may not be distinguished from AVHRR-imagery.

>From the AMSU-*RGB*-image (Figure 10, lower left panel) one can identify a navigation offset of the AMSU as compared to the contours of land mask (see for example the position of the island of Gotland). This navigation offset causes the likelihood for light precipitation at the eastern coast of Sweden to be non-zero, although from the AVHRR-imagery the area can be identified to be entirely cloud-free. This is the direct result of the mis-navigation, where especially pixels which are falsely assigned towards more open water surfaces are assigned a too high probability of precipitation. However, note that the associated probability that these pixels are precipitating (class 3) does never exceed 20% and most pixels are assigned to be most likely precipitation-free (class 1). Interestingly the mis-navigation is not apparent in the AVHRR-imagery, which indicates that in this case it may be a problem associated with the AMSU processing rather than with the spacecraft location or orientation.

4.2 Case 2

Case 2 (Figure 11) shows a wide-spread frontal precipitation event. It was observed on September 22nd, 1999 at 17:24 UT. Over the Baltic Sea the precipitation is again organised in bands, which are resembled in the AMSU-data as well. Comparing Figure 11 with Figure 10 only very few blue areas can be identified. Most of the precipitating areas have a highest probability to belong to class 2, and thus precipitation intensity might not exceed 5 mm/h. This is consistent with what is expected for widespread frontal precipitation events.

Another interesting feature are the false precipitation signals received from some of the Finnish radars which origin from a non-optimal quality

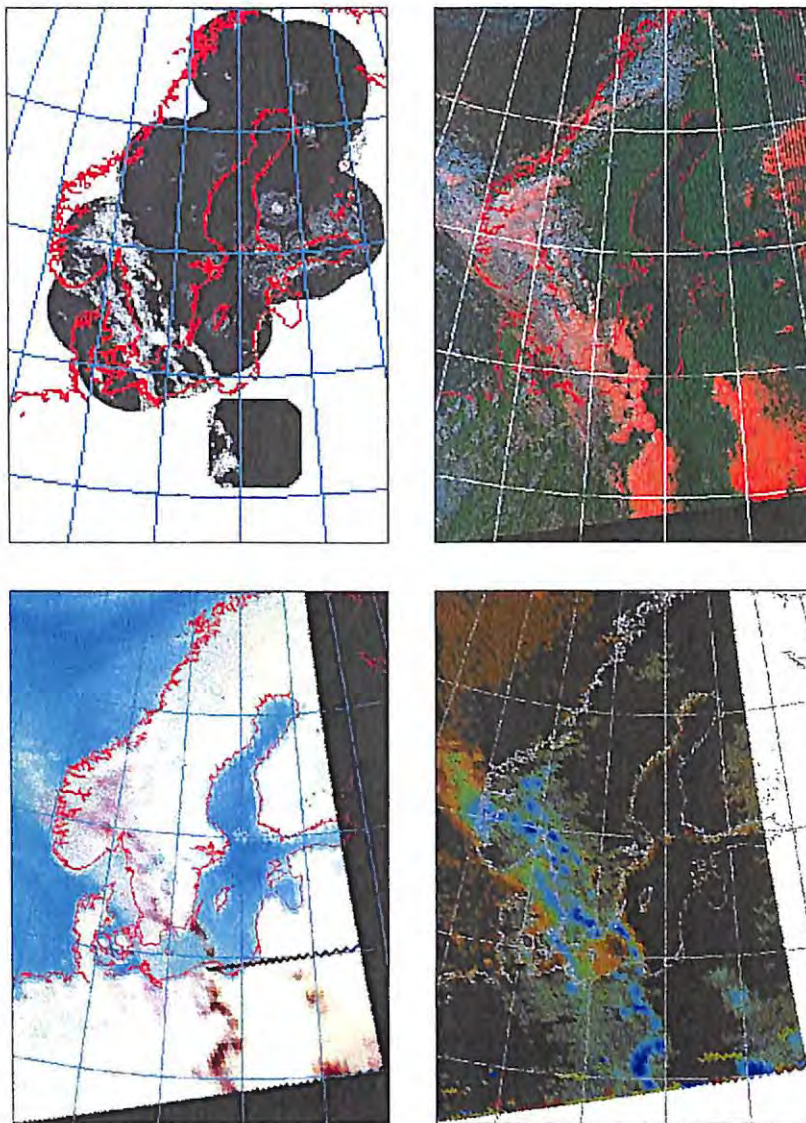


Figure 10: Visualization of the precipitation classification for June, 28th 1999, 17:45 UT. The upper left image shows the radar reflectivity observed from the BALTRAD network. The upper right image shows an rgb-composite of the AVHRR channels 1 (red), 2 (green), and 4 (blue). The lower left image shows an rgb-composite of the AMSU-B channels at 89 GHz (red), 150 GHz (green), and 183 ± 7 GHz blue. The lower right image gives the result of the precipitation classification, where the class 1 (risk for precipitation) is assigned red, class 2 green, and class 3 blue.

control of the Finnish radars. While for such obvious cases we excluded the false data from the data analysis in section 3, it highlights the problems associated with the use of radar data as ground truth for passive microwave remote sensing.

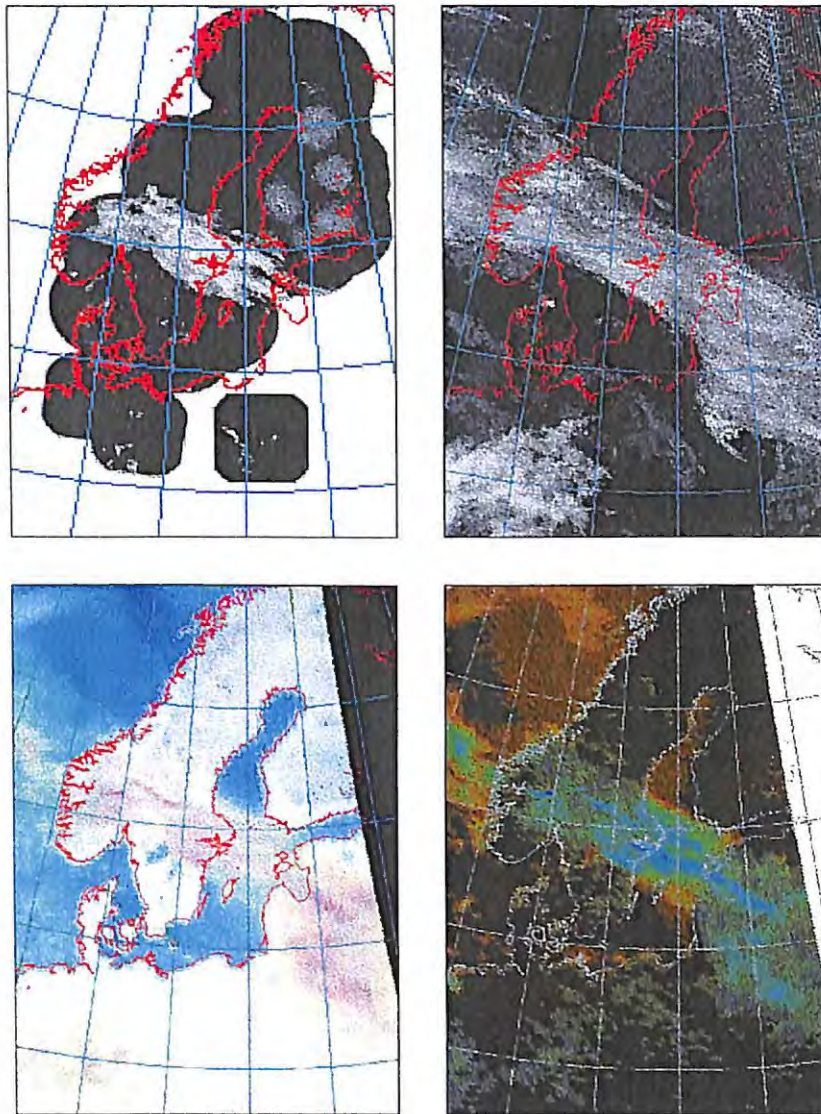


Figure 11: As Figure 10, but for the 22rd of September 1999, 17:46 UT.

In Figure 11 Denmark, Germany, and the southern part of Sweden appear to be almost precipitation-free with the exception of very few isolated precipitation events to be seen in the radar data. Although some of them are identified as such from the passive microwave, especially in the vicinity of coastlines it appears to be impossible to distinguish actual small-scale precipitation features from those of e. g. the above discussed false navigation. When comparing the scale of a few kilometers of those precipitation events to the much larger spatial scale of the passive microwave observations it is clear that a few percent of sub-pixel coverage with precipitation may result in ambiguities.

4.3 Case 3

Case 3 (Figure 12) was observed on September 23rd, 1999 17:46 UT, thus a day later than case 2. Two different precipitation areas can be observed for this day. The southern part of the Baltic region is covered with a narrow band of intensive precipitation, whereas more widespread frontal precipitation is found in the northern part. Both the light and the intensive precipitation are picked up by the AMSU and can also be distinguished very clearly.

The small convective cells observed in the AVHRR-imagery over the North Sea are apparently also associated with light precipitation. In the very northern part of the area, west of Norway, a large region is assigned to have a risk of precipitation (class 1), although the AVHRR-imagery suggests there might only be low clouds, if any. Surface observations taken from weather maps show overcast conditions with drizzle starting at approximately 68 degrees north, while between 66 degrees and 68 degrees only very few clouds were reported. It is thus likely that the extend of the area with risk for precipitation is over-estimated by the AMSU.

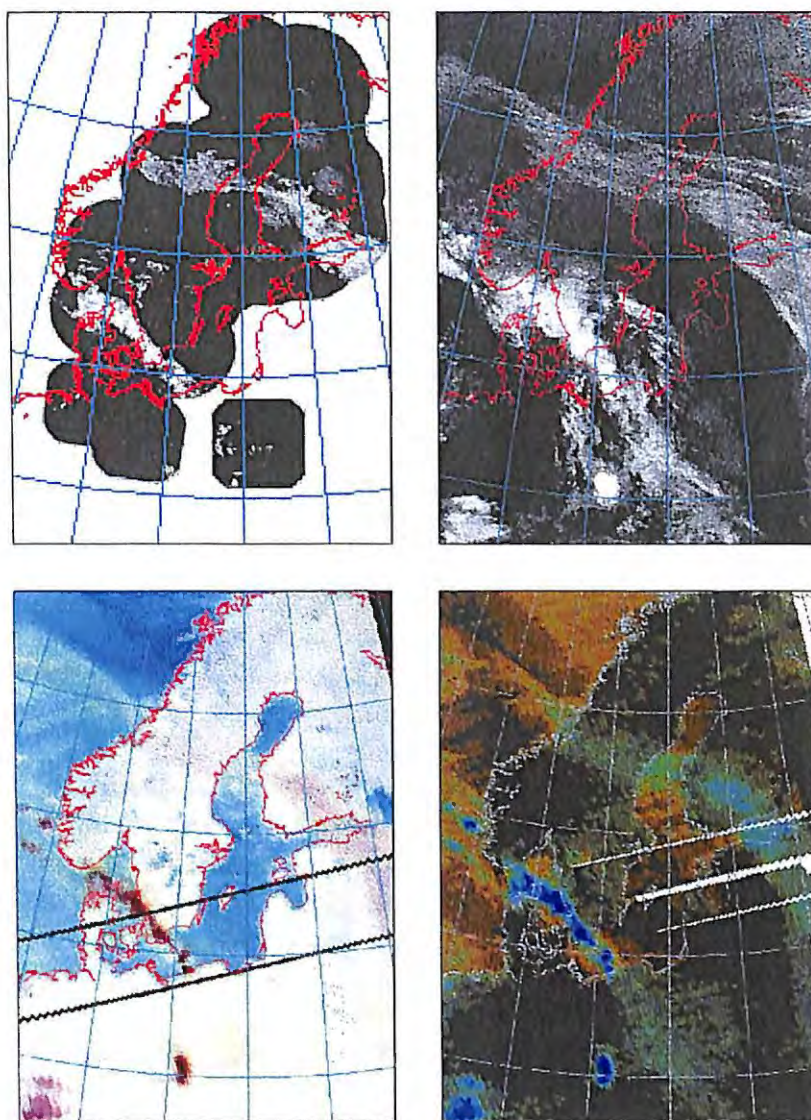


Figure 12: As Figure 10, but for the 23rd of September 1999, 17:24 UT.

5 Summary and conclusions

We describe a set of algorithms to identify precipitation and classify it according to its intensity. This product is designed for nowcasting applications. To account for the ambiguities in precipitation retrieval for instantaneous observations, we assign each observation a set of four probabilities associated with the likelihood of a given precipitation intensity. This approach allows the user to identify precipitation at different intensities and at the same time gives an estimate of the degree of accuracy of the classification.

The method is based on an eight month dataset of combined radar and AMSU data, which has been collected for the Baltic region during the period April to November 1999. While the extend of this area is quite limited, the Baltic region poses many specific requirements on algorithm development. First, the inhomogeneity of the surface has to be accounted for in algorithm development. In our algorithm this is solved using explicit information about the land/water distribution within the AMSU field of view. Second, the usually low precipitation intensities observed at high latitudes require a high accuracy of the identification algorithms. In this context we found that the AMSU-B channel at 150 GHz is advantageous since it allows to identify precipitation to a significantly higher accuracy than the channel at 89 GHz.

While the product is derived on a comparably large dataset, the entirely statistical approach used in this investigation of course requires further monitoring of the products. Especially the following issues have to be addressed.

- The identification of snow and/or sea ice could not yet be verified on a statistically significant basis from the current dataset. Although the results for the few cases with snow cover were quite promising, an extension of the development and validation database to winter cases is considered necessary.
- The transfer of the here-presented algorithms to other climate areas might need some adjustment. This, however, can be done straight forward, since as a first step only the corrections of the scattering index to a zero mean for precipitation-free areas are to be adjusted. In a second step the likelihood functions of different precipitation intensities might be adjusted as well.

In future work we will address both of these topics. The dataset will be extended to cover at least one year of data and for the winter time conditions the accuracy in delineating ice and snow covered surfaces will be investigated. To further investigate the methods capabilities under different

climate conditions it is planned to transfer it to Spain, where both, precipitation type and land surface characteristics are different from those in the Baltic region.

References

- Adler, R., A.J.Negri, P.R.Keehn, and I.M.Hakkarinen, Estimation of monthly rainfall over japan and surrounding waters from a combination of low-orbit microwave and geosynchronous ir data., *J. Appl. Meteorology*, 32, 335–356, 1993.
- BALTEX, The main baltex experiment 1999-2001 - bridge. strategic plan, *Publication No. 9*, International BALTEX Secretariat, GKSS Research Center, Geesthacht, 1997.
- Bauer, P., and N. C. Grody, The potential of combining ssm/i and ssm/t2 measurements to improve the identification of snow cover and precipitation, *IEEE Trans. Geosci. Remote Sensing*, 33, 252–261, 1995.
- Bennartz, R., On the use of ssm/i measurements in coastal regions., *J.Atmos. Oceanic Technology*, 16, 417–431, 1999a.
- Bennartz, R., Optimal convolution of amsu-a to amsu-b, *J.Atmos. Oceanic Technology*, in press., 1999b.
- Bennartz, R., and D. B. Michelson, Correlation of precipitation estimates from spaceborne passive microwave sensors and weather radar imagery for baltex pidcap, *Int. J. REMote Sensing.*, 1999, (submitted).
- Bennartz, R., and G. Petty, The sensitivity of microwave remote sensing observations of precipitation to ice particle size distributions, *J. App. Met.*, 1999, (submitted).
- Bennartz, R., A. Thoss, and J. Fischer, Retrieval of precipitation and columnar water vapour path from amsu-a/b, *Proc. IX TOVS study conference, Igly, Austria, 20-26 February 1997*, 1997, 11–20.
- Brandt, R., C. Collier, H.-I. Isemer, J. Koistinen, B. Macpherson, D. Michelson, S. Overgaard, E. Raschke, and J. Svensson, Baltex radar research - a plan for future action, *Publication No. 6*, International BALTEX Secretariat, GKSS Research Center, Geesthacht, 1996.
- Dybbroe, A., A. Thoss, and K.-G. Karlsson, The avhrr cloudmask scheme of te safnwc, *Proceedings of the 1999 EUMETSAT Satellite Data Users Conference*, in press, 1999.

- Goodrum, G., K. B. Kidwell, and W. W. eds, eds., *NOAA KLM User's Guide*, NOAA, 1999.
- Grody, N. C., Classification of snow cover and precipitation using the special sensor microwave/imager, *J. Geophys. Res.*, 96, 7423–7535, 1991.
- Grody, N. C., F. Weng, and R. Ferraro, Application of amsu for obtaining hydrological parameters, *Proc. of the fourth conference on microwave radiometry, Florence, Italy, March 1999, in press*, 1999.
- Karlsson, K.-G., A. Thoss, and A. Dybbroe, High resolution cloud products from noaa avhrr and amsu, *EUMETSAT Proceeding of the SAF Training Workshop - Nowcasting and very short range forecasting*, ISBN 92-91 10-030-7, 180–190, 1999.
- Klaes, K. D., Atovs processing in europe, *Proceedings of the Ninth International TOVS Study Conference*, pp. 267–274, 1997.
- Koistinen, J., and T. Puhakka, An improved spatial gauge-radar adjustment technique, in *Proc. 20th Conf. on Radar Met.*, pp. 179–186, AMS, 1981.
- Michelson, D., T. Andersson, C. Collier, Z. Dziewit, J. Koistinen, S. Overgaard, J. Riedl, and V. Zhukov, The international radar network for the baltic sea experiment, in *Preprints 29th Int. Conf. on Radar Met.*, pp. 317–320, AMS, 1999.
- Michelson, D. B., Baltex radar data centre products and their algorithms, *Rmk*, SMHI, S-601 76 Norrköping, Sweden, 2000, (in prep.).
- Smith, E. Lamm, R. Adler, J. Alsihouse, K. Aonashi, E. Barrett, P. Bauer, W. Berg, A. Chang, R. Ferraro, J. Ferriday, S. Goodman, N. Grody, C. Kidd, D. Kniveton, C. Kummerow, G. Liu, F. Marzano, A. Mugnai, W. Olson, G. Petty, A. Shibata, R. Spencer, F. Wentz, T. Wilheit, and E. Zisper, Results of wetnet pip-2 project., *Journal of the Atmospheric Sciences*, 55, 1483–1536, 1998.
- Spencer, W., H. Goodman, and R. Hood, Precipitation retrieval over land with the ssm/i: Identification of the scattering signal., *J. Atmos. Oceanic Technology*, 6, 254–273, 1989.

A Algorithm description for scattering-based precipitation identification

A.1 Land

Over land surfaces two different algorithms are employed, dependent on whether only the AMSU-B footprint can be considered as homogeneous land, or also the surrounding AMSU-A footprint.

A.1.1 AMSU-A water or coast, AMSU-B land:

$$s_{l1} = (T_{89} - T_{150}) - (0.158 + 0.0163\theta) \quad (1)$$

where θ , given in degrees, is the zenith angle of the observation. The last term corrects for the weak dependence of the difference of the brightness temperatures on zenith angle. We found it empirically by regressing s for all precipitation-free observations against the local zenith angle.

A.1.2 AMSU-A land (and AMSU-B land):

$$s_{l2} = (T_{23} - T_{150}) - (-1.7428 + 0.0776\theta) \quad (2)$$

where θ , given in degrees, is the zenith angle of the observation. As before, the last term corrects for the weak dependence of the difference of the brightness temperatures on zenith angle.

A.2 Sea

A.2.1 AMSU-A land or coast, AMSU-B water:

$$s_{s1} = (T_{89} - T_{150}) - (-39.2010 + 0.1104\theta) \quad (3)$$

where θ , given in degrees, is the zenith angle of the observation. The last term corrects for the dependence of the difference of the brightness temperatures on zenith angle. Note, that there is a considerable offset between T_{89} and T_{150} over water which is also corrected for. This correction is probably the least general part of the set of algorithms, since it is supposed to be strongly dependent on e. g. the water vapour path and atmospheric temperature and may thus not be valid for other regions with completely different atmospheric conditions, such as the tropics. It can, however, easily be generalized by adjusting the offset to the observed mean difference between T_{89} and T_{150} for a given area.

A.3 Coast

The algorithm we use for coast is a mixture of the land (Eqn. 1) and sea (Eqn. 3) algorithms:

$$s_c = (1 - l)s_{s1} + ls_{l1} \quad (4)$$

where l is the fraction of land in the AMSU-B footprint, s_{s1} is the scattering index derived from Equation (3) and s_{l1} is the scattering index derived from Equation (1). The weighted average according to the fraction of land in the footprint also automatically weights the zenith angle and offset corrections for the land and sea parts, so regardless of the fraction of land in the footprint, a precipitation-free scene has an average scattering index of 0 K.

B Software and data formats

This section holds a short description of the software which was developed during the visiting scientist stay and of the output data formats of the retrieval. The software can be divided into two parts, one which handles the spatial degradation and convolution of a land/sea-mask to the AMSU's resolution to discriminate between different surface types. The other part is the retrieval itself.

B.1 Convolution of land/sea-mask

Convolved land/sea-masks are used in the retrieval to separate different surface types. The convolution is done for both, AMSU-A and AMSU-N separately. The convolution is performed by the following void functions which are coded in `convolve.c`:

```
void convolve_lsm_b(
  AMSU_B_1C_header *amsu_b,
  float **lsm_b)
void convolve_lsm_a(
  AMSU_A_1C_header *amsu_a,
  float **lsm_a)
```

where the input structures `amsu_a` and `amsu_b` are defined in the `ahamap` software of the SMHI. The output fields `**lsm_a` respective `**lsm_b` are two-dimensional fields of the size of the input brightness temperatures in the `ahamap` `amsu` structures. Note, that the input structures have to be provided from the calling program. The output fields `lsm_a` and `lsm_b` have to be allocated and freed in the calling program. A sample program to use the convolution is provided in `conv_test.c`.

Name	Type/Dimension	Explanation
amsu_a	ahamap structure	AMSU-A data
amsu_b	ahamap structure	AMSU-B data
pulse	1D, AMSU-B scanlines	holds
closest_a_x	2D: AMSU-B field size	holds closest AMSU-A scan position for all AMSU-B pixels
closest_a_y	2D: AMSU-B field size	holds closest AMSU-A scan line for all AMSU-B pixels
tbconv	3D: channels× AMSU-A field size	holds convolved AMSU-B data
flag_b	2D AMSU-B field size	Flag, see Table 9

Table 7: Input and output data for Backus-Gilbert convolution

The convolution relies on a land/sea-mask which is provided in the same directory as the above programs. It is currently restricted to Europe, north of 40 degrees north. Correctly convolved pixels are assigned values between zero (homogeneous water surface) and one (homogeneous land surface). Pixels outside the area of the land/sea-mask are assigned a value of -1.

B.2 Backus-Gilbert convolution of AMSU-B to AMSU-A

A fast method to convolve AMSU-B to AMSU-A is provided. This method is documented in detail in *Bennartz (1999b)*. Although not used in the precipitation retrieval itself, it has been used for quality control of the AMSU-B data before the radio frequency interference problems on NOAA-15 have been solved (before September 1999). The Backus-Gilbert convolution is implemented in `bg_amsu_b.c`:

```

void get_sync_pulse(
AMSU_A_1C_header *amsu_a,
AMSU_B_1C_header *amsu_b,
int *pulse,
int **closest_a_x,
int **closest_a_y)
void convolve(
AMSU_A_1C_header *amsu_a,
AMSU_B_1C_header *amsu_b,
int *pulse,
float ***tbconv,
unsigned char **flag_b)

```

All input and output fields are listed in Table 7.

All input and output fields have to be allocated, provided and freed by the calling program. For an example see `ret_test.c`.

B.3 Retrieval software

The following four void functions are used for retrieval:

```
void retrieve_wvp(
    AMSU_A_1C_header *amsu_a,
    float **wvp,
    unsigned char **flag_a)
```

Retrieves columnar water vapour path over water surfaces from AMSU-A 23.8 and 31.4 GHz. Additional input (regression coefficients) is provided in `wvpcoeffs.dat`. Structure `amsu_a` input, 2d-fields `wvp` output, `flag_a` input/output, both fields have the size of the AMSU-A images.

```
void retrieve_lwp(
    AMSU_A_1C_header *amsu_a,
    float **lwp,
    unsigned char **flag_a)
```

Retrieves columnar water vapour path over water surfaces from AMSU-A 23.8 and 31.4 GHz. Additional input (regression coefficients) is provided in `lwpcoeffs.dat`. Structure `amsu_a` input, 2d-fields `lwp` output, `flag_a` input/output, both fields have the size of the AMSU-A images.

```
void retrieve_si_new(
    AMSU_A_1C_header *amsu_a,
    AMSU_B_1C_header *amsu_b,
    float **lsm_a,
    float **lsm_b,
    float **si_b,
    unsigned char **flag_a,
    unsigned char **flag_b)
```

Retrieves scattering index at AMSU-B resolution. Except `si_b` all fields are input. The flags `flag_a` and `flag_b` are both, input and output.

```
void classify_hist(
    AMSU_B_1C_header *amsu_b,
    float **si_b,
    float **lsm_b,
    unsigned char **flag_b,
    float **m0,
    float **m1,
    float **m2,
    float **m3)
```


Variable	Description	Unit	Dimension
wvp	Water vapour path	$[kg/m^2]$	AMSU-A field
lwp	Liquid water path	$[kg/m^2]$	AMSU-A field
si	scattering index	$[K]$	AMSU-B field
flag_a	Flags, see Table 9		AMSU-A field
flag_b	Flags, see Table 9		AMSU-B field
lsm_a	convolved land/sea-mask	[1]	AMSU-A field
lsm_b	convolved land/sea-mask	[1]	AMSU-B field
m0	probability class 1 (Table 2)	[1]	AMSU-B field
m1	probability class2 (Table 2)	[1]	AMSU-B field
m2	probability class3 (Table 2)	[1]	AMSU-B field
m3	probability class 4 (Table 2)	[1]	AMSU-B field

Table 8:

The program classifies the retrieved scattering index according to the above Table 2 in classes, which are on output found in m0–m3, where m0 holds the probabilities for class 1, m1 that of class 2 and so forth.

As before all input and output fields have to be provided from the calling program. A sample program that performs the retrieval can be found in `ret_test.c`.

Table 8 lists the results of the retrieval

B.4 Flags

Besides the retrieval results a set of flags are produced for both the AMSU-A and the AMSU-B products. These flags are used internally to handle different exceptions.

Flag	Value	Explanation
F_OCEAN	1	pixel is over ocean
F_COAST	2	mixed surface
F_LAND	4	pixel is over land
F_WVP_FAIL	8	water vapour retrieval failed (ocean)
F_LWP_FAIL	16	liquid water retrieval failed (ocean)
F_SI_FAIL	32	scattering index failed

Flag	Value	Explanation
F_OCEAN	1	pixel is over ocean
F_COAST	2	mixed surface
F_LAND	4	pixel is over land
F_BG_FAIL	8	Backus-Gilbert convolution failed
F_ICE	16	ice surface detected
F_SI_FAIL	32	scattering index failed
F_SI_INCLUDES_A	64	scattering index includes AMSU-A observations

Table 9: Flags for AMSU-A products (upper Table) and AMSU-B products (lower Table)

